# Dose-related microstructural changes in metastatic patients measured with diffusion MRI: First insights of the APRICOT trial

Elixabete Ansorena

## ABSTRACT

**Background:** Radiotherapy (RT) is one of the most common therapeutic intervention for cerebral tumor, which also promotes changes in healthy brain structures, leading to cognitive decline in the majority of the patients. In this study, we aim to evaluate the changes in brain microstructure as a result of radiation delivery by means of diffusion MRI (dMRI).

**Methods:** We selected 9 metastatic patients from the APRICOT trial who underwent both pre-RT and post-RT DWI and T1 scans. We estimated the diffusion metrics for a total of 31 white matter pathways and then evaluated their change as a function of the received dose (%/Gy).

**Results:** The largest FA and AFD decreases were recorded in the Right Inferior Longitudinal Fasciculus, 7,84 %/Gy and the Left Uncinate Fasciculus, 61,09 %/Gy. Regarding the diffusivities, the Right Corticospinal Tract increased the most for all three metrics, MD, AD and RD 4,76 %/Gy, and 5,02 %/Gy and 7,47 %/Gy respectively.

**Conclusion:** Diffusion metrics are susceptible to radiation delivery, AFD presenting the most notable changes. These findings imply the use of dMRI in better understanding the mechanisms behind structural changes, which may lead to cognitive decline.

## I. INTRODUCTION

Radiotherapy (RT) is one of the primary treatment options for brain malignancies based on the delivery of radiation to brain areas affected by tumour cells. RT is usually combined with surgery, which primary role is the reduction of tumour mass. First, if the location allows it, the majority of the tumour is removed via surgery. This procedure does not ensure that all affected cells have been removed. Therefore, in order to treat all remaining tumour cells and avoid a relapse on tumour growth, RT is employed.

RT treatment is preceded by RT planning, a procedure where target areas, such as the gross tumour volume (GTV), are identified, and the dose delivery settings are defined. Furthermore, RT is not a selective treatment, meaning it damages both healthy and tumour cells alike, highlighting the importance of RT planning when defining beam trajectories.

Regardless of radiation delivery precision, healthy tissue will always receive some amount of radiation, leading to various forms of tissue decay. Examples of physical changes include cortical thinning and white matter abnormalities, such as necrosis and demyelination [1]. Consequently, these effects on brain structure can result in cognitive decline, a radiotherapy side effect manifested in almost the entirety of patients that have undergone said procedure.

The generalized cognitive decline, and consequent quality of life impairment, of RT patients emphasises the need for a better understanding of the effects of after radiation delivery to the brain. Previous research on the field of radiation-related cognitive decline has been mainly focused on measuring volumetric variations on grey matter (GM) by means of T1 MR image analysis. As a result, these studies are purely location-based, meaning that cognitive decline will be concluded if and only when a specific cortical area related to a task showcases a reduction in geometric measures, such as volume.

Although these studies have gathered promising results [2], they are all failing to consider a key parameter, brain connectivity through white matter (WM). WM is responsible for connecting different GM areas and transmitting information from the cortex to other parts of the body. Therefore, solely focusing on a GM location-based approach does not account for the changes in microstructure that might trigger further cognitive decline as a result of WM pathway decay.

In this work, we evaluate the effect of RT on brain microstructure using diffusion magnetic resonance imaging (dMRI). We examine tissue changes per white matter pathways, which will shed some light on the previously unconsidered RT effects.

## II. METHODS

### A. Patient Selection

All patient data used in our study was provided by the APRICOT trial and acquired between October and December of 2021. Subjects underwent pre-surgery T1 and DWI, treatment planning CT, and follow-up T1 and DWI scans three months after RT. A total of 16 eligible patients were identified. Furthermore, we selected subjects who had undergone a single RT session, resulting in 9 patients. All selected final subjects received very similar RT treatments: five of them 1x24 Gy, two 1x21 Gy and one 1x18 Gy.

### B. Image Acquisition

All MRI scans, T1 and DWI, were acquired on a 3T Philips Ingenia scanner (Philips Medical Systems). More specifically, the T1 scans were captured via non-enhanced 3D turbo-spin echo (TSE) sequence (TR = 8.1 ms, TE = 3.7 ms) with a voxel resolution of 1x1x1 mm.

The DWI scans were acquired with spin-echo echo planar imaging (SE-EPI) (TR = 4.55 s, TE = 86 ms) and voxel resolution of 2x2x2 mm with 40 directions of b=1000 s/mm$^2$ and 6 b=0 s/mm$^2$ scans.

The planning CTs were acquired via the Brilliance Big bore scanner (Philips Medical Systems) using a matrix size of $512 \times 512$ and 0.65x0.65x1 mm voxel size.

### C. Image Pre-processing

All images were pre-processed with FMRIB Software Library (FSL) [3], Computational Anatomy Toolbox (CAT12) [4], Statistical Parametric Mapping (SPM) [5], ExploreDTI [6] and MRIToolkit [7].

First, the field of view (FOV) of the T1 images were reduced to contain only the head using FSL's "robustfov". Next, we ran the "affine pre-processing pipeline" of CAT12 on the FOV-reduced T1 images with the default settings, which include bias-field, noise and global intensity corrections. Last, baseline and follow-up anatomical T1 scans were rigidly coregistered with 6 degrees-of-freedom, defining a common space for the analysis to take place.

Next, the pre-processing of the diffusion scans was conducted, which consisted on performing MP-PCA denoising [8] followed by Subject Motion, Eddy Current and Susceptibility-Distortion correction [9]. Susceptibility-distortion correction was conducted based on the coregistered T1 images, consequently transforming the processed DWI scan into the coregistered T1 space. Any rotation of the DW images were subsequently followed by realigning the B-matrices as well [10].

Furthermore, the CT images were cropped as well to improve the registration outcome and reduce computational time. As a result, the neck, shoulders, and any other treatment equipment (e.g.: head position fixture) was excluded from the FOV. This exact procedure was repeated and applied for the dose and tumour volume (TV) maps for each patient. Finally, we rigidly registered the CT, GTV and dose information to the already pre-processed T1 space to ensure spatial coherence throughout all the data. Moreover, based on the RT planning data, we calculated the equivalent dose in 2 Gy per fraction (EQD2), which will later be used to calculate the mean dose received by each tract.

### D. Modelling and Tractography

First, we performed the DTI fit based on the Ordinary Least Squares method. Next, in order to compute the tractography, we modelled the diffusion signal using the Generalised Richardson Lucy (GRL) algorithm [11] to estimate the fibre orientation distribution (FOD) in each voxel. GRL has shown improved performance compared to other models such as Diffusion Tensor Imaging (DTI), providing superior detection capability for crossing fibres and computing automatic tissue segmentation as showcased in Figure 1.
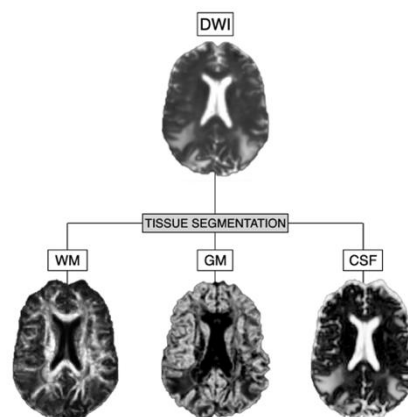


*Figure 1:Tissue segmentation based on diffusion data*

Moreover, GRL is proficient in accounting for free water components, succeeding to model the diffusion signal even in the presence of edema. Figure 2 further depicts this property.
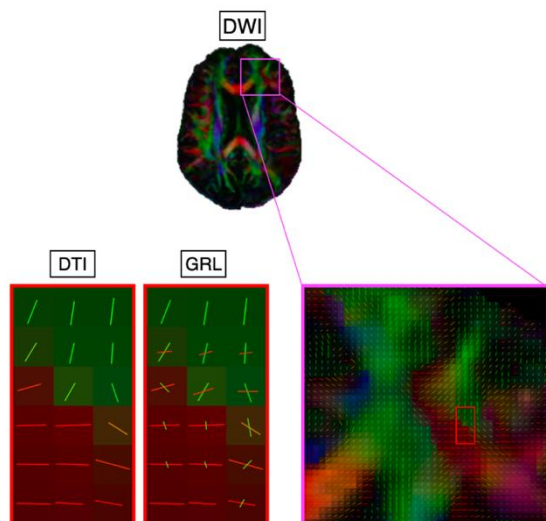
2

*Figure 2: DTI and GRL comparison for fibre crossing detection*

After the calculation of the FODs, the tractography was computed. By anatomical definition, white matter pathways connect grey matter regions through white matter, meaning there should not be any tracts outside of those bounds. Based on this principle, GRL can terminate the tracts on the GM-CSF interface to ensure anatomical accuracy as seen on Figure 3. As a result, we obtained a GRL-based and anatomically constrained whole brain tractography (WBT).
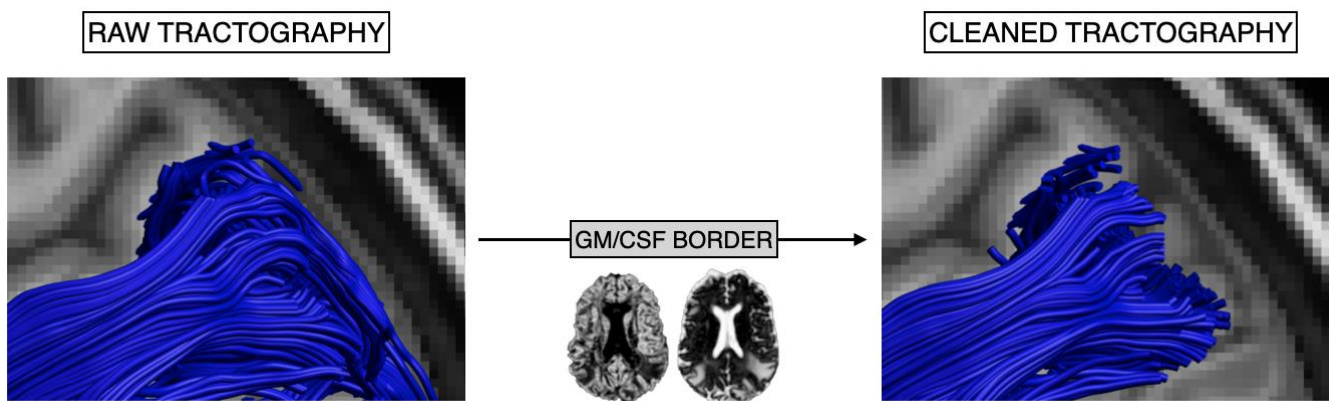
## E.  Brain Parcellation

Brain parcellation is a key step that will enable the detection of 181 different GM/WM via Freesurfer (FS) [12] brain regions which will be used as input for the eventual automatic region-based tract segmentation.

However, when dealing with not-healthy participants like the current patient population, the data presents multiple lesions corresponding to tumour and edema, hindering the proper parcellation of the brain. The presence of lesions lead to abnormal brain structures or a change in local T1 contrast, either darkening or lightening the intensities of otherwise healthy tissue. As a result, the default parcellation algorithm is not able of recognizing these lesion-affected areas as brain tissue and the parcellation cannot be fully completed.

In order to solve this problem, Virtual Brain Grafting (VBG) [13] is used, which replaces the lesion-affected areas with synthetic healthy brain tissue from a template brain, consequently aiding the FS algorithm to perform a successful parcellation. By the end of the FS based parcellation, the artificially inserted areas are replaced with the original ('lesion') label.

As shown in the parcellation pipeline on Figure 4, the VBG algorithm together with FS succeeded on performing a satisfactory parcellation of GM and WM regions of the brain. The resulting map contains 181 labels based on the Destrieux atlas [14] corresponding to different brain regions and a specific label representing the abnormalities.
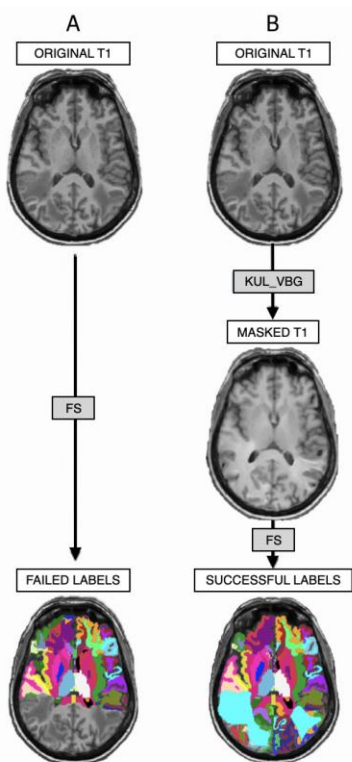


*Figure 3: Tract clean-up based on GM/CSF border*

*Figure 4: A) Incorrect parcellation due to tissue abnormalities. B) Correct parcellation due to tissue replacement*

## F. Automatic Region-Based Tract Segmentation

The whole brain tractography and parcellation were combined in a MATLAB algorithm that enables the extraction of 50 white matter tracts based on anatomical connectivity. We designed the algorithm based on a set of inclusion/exclusion criteria [15] that defined the connectivity between brain regions through white matter pathways.
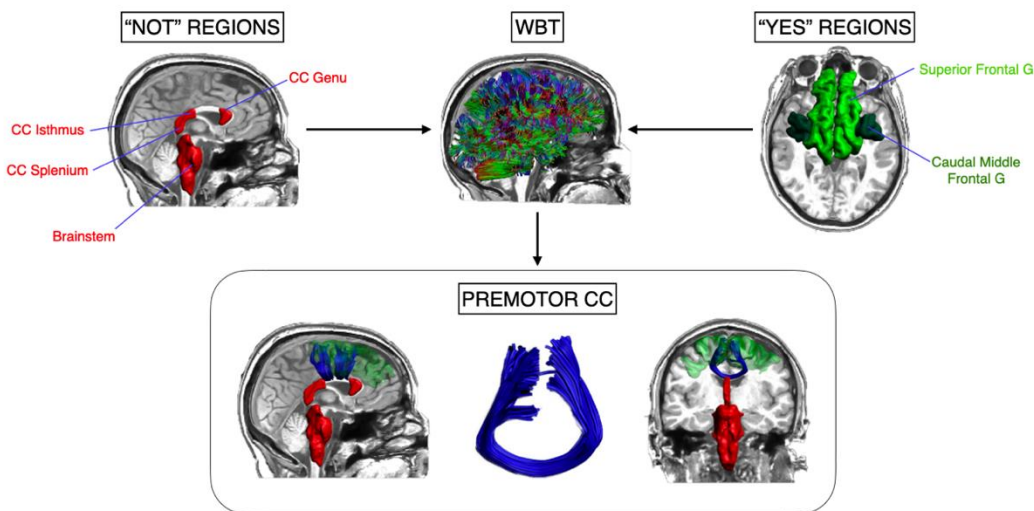
This principle of tract segmentation ensures all resulting tracts are anatomically accurate and connect functionally related brain regions.

Figure 5 showcases the example of the Premotor Corpus Callosum (CC), which segmented tracts define the right-left hemispherical connectivity between regions such as the Caudal Middle Frontal and Superior Frontal Gyrus, displayed in green. Moreover, exclusion regions, coloured red, include the Brainstem and CC subsections of the Splenium, Isthmus and Genu to ensure the elimination of stray tracts.

## G. Statistical Analysis

Out of the segmented 50 white matter tracts, 19 were rejected due to reconstruction inaccuracies as a result of poor data quality and overall detection difficulty of the tracts. Thus, the statistical analysis has been conducted on 31 tracts per patient and timepoint.

Aiming to analyse the unique effect of dose on brain microstructure, we eliminated those instances of tracts that might have been directly affected by the tumour, edema, or surgery from the analysis. This step ensured that all measured changes would be a consequence of solely the radiation delivery.

By means of the automatic tract segmentation algorithm, we computed the diffusion metrics for each individual tract, mean FA, MD, AD, RD and AFD for instance.



*Figure 5: Example of NOT and YES region usage for automatic tract segmentation of the Premotor CC*

4

Next, we defined the exact radiation received by each tract. We achieve this by mapping the dose information into the segmented tracts, as shown in Figure 6.
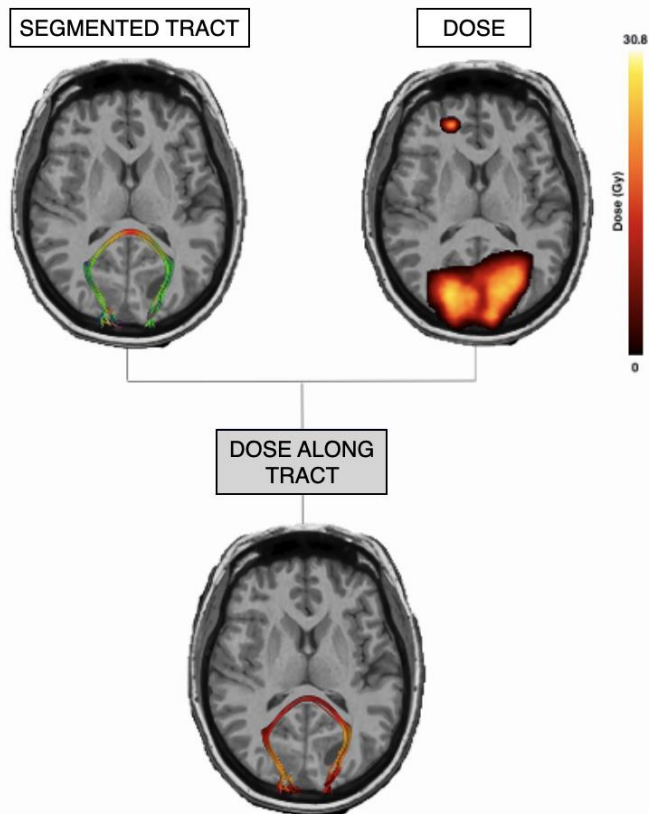


*Figure 6: Dose mapping along segmented Occipital CC*

As displayed in the previous figure, a single tract can have various hotspots of dose delivery while other areas barely receive any radiation. Taking this into account, instead of evaluating dose effect on diffusion metrics for the entirety of the pathway, we opted to perform an along-the-tract statistical analysis [16] to make sure focal effects were not averaged out.

This approach is based on collapsing the entire tract into a single mean fibre and then resampling that into many discrete sections. In our case, we decided to resample all tracts into 86 points, which corresponds to the average path length of all our subjects. Figure 7 further depicts this method.
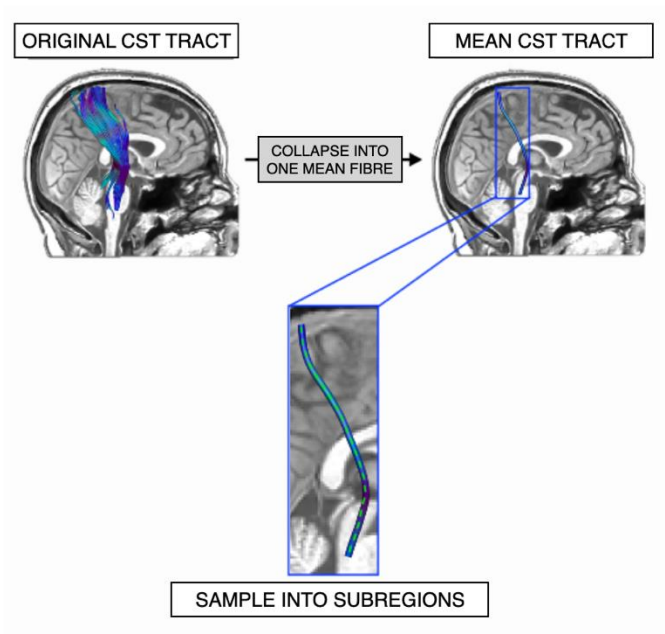


*Figure 7: Mean fibre and sampling of the CST*

Next, we performed a regression analysis to estimate the diffusion parameter change before and after RT as a function of received dose per Gy in each of the sampled 86 points for all tracts and subjects.
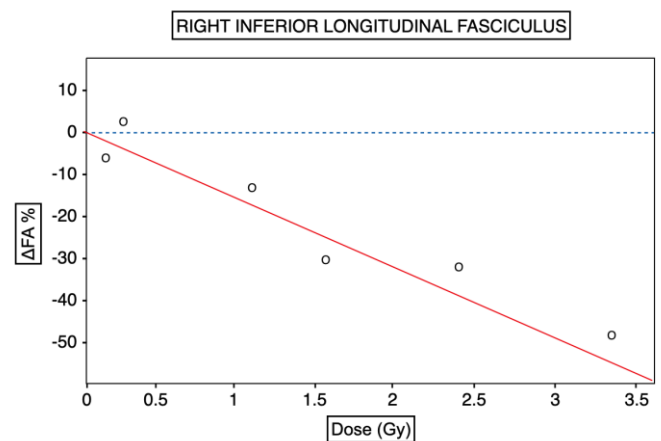


*Figure 8: Regression of 1 of 86 segments on the R-ILF*

In conclusion, Figure 9 summarizes the entire pipeline described in this section.
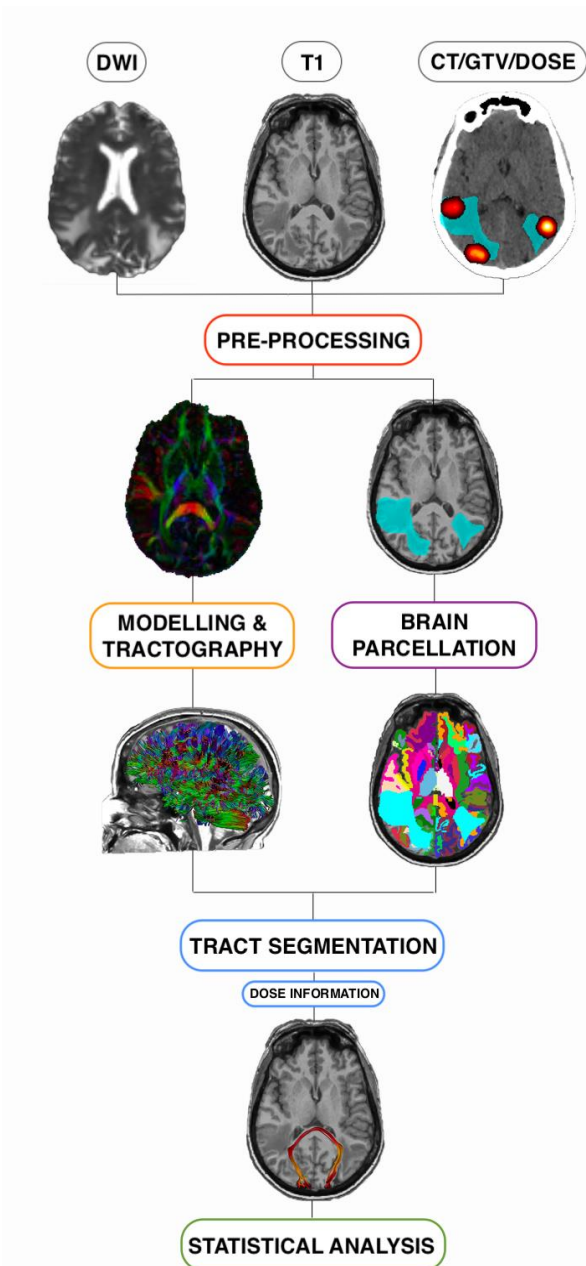
*Figure 9: Methods pipeline*

## III. RESULTS

Using a p-value of 0.05 as the threshold for statistical significance, relevant segments of each tract were identified to interpret the results from. As a result, we show that FA and AFD decreased in 56% and 75% of the tracts, while MD, AD and RD increased in 52%, 56% and 56% instances respectively. Table 1 displays the percentages of the tracts that showed significant change. For instance, the PMCC showed a decrease in FA in 12,79 % of the tract, while no increasing regions were recorded.

*Table 2: Percentage of significant change along tracts. Blue: largest increase. Red: Largest decrease*

|  | FA % | | MD % | | AD % | | RD % | | AFD % | |
|---|---|---|---|---|---|---|---|---|---|---|
|  | ↓ | ↑ | ↓ | ↑ | ↓ | ↑ | ↓ | ↑ | ↓ | ↑ |
| AF L | NaN | 9,30 | 6,98 | 5,81 | 1,16 | NaN | 10,47 | 3,49 | 10,47 | NaN |
| AF R | 1,16 | 5,81 | 3,49 | 12,79 | NaN | 15,12 | 4,65 | 6,98 | 25,58 | 10,47 |
| CC L | 4,65 | NaN | NaN | 4,65 | 2,33 | NaN | NaN | 20,93 | 34,88 | NaN |
| CC R | 1,16 | NaN | 5,81 | NaN | 3,49 | NaN | NaN | 1,16 | NaN | 2,33 |
| CST L | 6,98 | 5,81 | 20,93 | 4,65 | 9,30 | NaN | 6,98 | 2,33 | 31,40 | 1,16 |
| CST R | 3,49 | 4,65 | NaN | 2,33 | NaN | 4,65 | 1,16 | 2,33 | 2,33 | NaN |
| FA L | NaN | NaN | NaN | 5,81 | NaN | NaN | NaN | NaN | 33,72 | NaN |
| FA R | 1,16 | NaN | 1,16 | NaN | NaN | NaN | NaN | NaN | NaN | 9,30 |
| IFOF L | NaN | 4,65 | NaN | NaN | NaN | 4,65 | NaN | 1,16 | 10,47 | 3,49 |
| IFOF R | NaN | 9,30 | 6,98 | NaN | NaN | NaN | 15,12 | NaN | 2,33 | 4,65 |
| ILF L | NaN | NaN | NaN | 23,26 | 1,16 | NaN | 1,16 | NaN | 2,33 | NaN |
| ILF R | 8,14 | 6,98 | NaN | NaN | NaN | 6,98 | NaN | 1,16 | 2,33 | NaN |
| MLF L | 8,14 | NaN | NaN | 22,09 | NaN | 3,49 | NaN | 20,93 | 12,79 | 2,33 |
| MLF R | 8,14 | 2,33 | 4,65 | NaN | 10,47 | 2,33 | NaN | 4,65 | 10,47 | NaN |
| OCC | NaN | 8,14 | NaN | 2,33 | NaN | 1,16 | 8,14 | 2,33 | NaN | NaN |
| PCC | 1,16 | NaN | NaN | 5,81 | 1,16 | NaN | NaN | NaN | NaN | NaN |
| PTR L | 1,16 | NaN | NaN | NaN | NaN | NaN | NaN | NaN | NaN | 8,14 |
| PMCC | 12,79 | NaN | NaN | NaN | NaN | 2,33 | NaN | 15,12 | 13,95 | 2,33 |
| PSMCC | 9,30 | NaN | NaN | 12,79 | 1,16 | 8,14 | 1,16 | 10,47 | 29,07 | 1,16 |
| STR L | NaN | NaN | NaN | NaN | 5,81 | NaN | NaN | NaN | 2,33 | 6,98 |
| STR R | NaN | NaN | NaN | NaN | NaN | 4,65 | NaN | NaN | 2,33 | 1,16 |
| SMPT L | NaN | 2,33 | NaN | NaN | NaN | NaN | NaN | NaN | 25,58 | NaN |
| SMPT R | NaN | NaN | 1,16 | 10,47 | NaN | 2,33 | 1,16 | 3,49 | 1,16 | NaN |
| TPCB L | NaN | 1,16 | 2,33 | NaN | NaN | 6,98 | 8,14 | NaN | NaN | 16,28 |
| TPCB R | NaN | NaN | NaN | NaN | NaN | 4,65 | NaN | NaN | 5,81 | 1,16 |
| UF L | NaN | NaN | 11,63 | NaN | 5,81 | NaN | 32,56 | NaN | 18,60 | NaN |
| UF R | NaN | 4,65 | 4,65 | NaN | 4,65 | NaN | 5,81 | NaN | 2,33 | NaN |
| WPT L | NaN | 3,49 | 4,65 | NaN | 1,16 | NaN | 4,65 | NaN | 32,56 | 1,16 |
| WPT R | 3,49 | 1,16 | NaN | 5,81 | 1,16 | 15,12 | NaN | 6,98 | NaN | NaN |
| WSLF L | NaN | NaN | 2,33 | 4,65 | NaN | 2,33 | NaN | 3,49 | 8,14 | NaN |
| WSLF R | 4,65 | 3,49 | 3,49 | 2,33 | NaN | NaN | 5,81 | NaN | NaN | 1,16 |

Moreover, the following Table 2 presents the mean changes recorded in the statistically significant regions of the tracts.

*Table 1: Mean change along tracts as a funciton of dose. Blue: Largest increase. Red: largest decrease.*

|  | FA %/Gy | | MD %/Gy | | AD %/Gy | | RD %/Gy | | AFD %/Gy | |
|---|---|---|---|---|---|---|---|---|---|---|
|  | ↓ | ↑ | ↓ | ↑ | ↓ | ↑ | ↓ | ↑ | ↓ | ↑ |
| AF L | NaN | 6,84 | 2,95 | 1,91 | 2,76 | NaN | 3,67 | 0,85 | 27,85 | NaN |
| AF R | 0,60 | 3,84 | 0,67 | 2,00 | NaN | 2,89 | 0,85 | 2,73 | 14,21 | 52,95 |
| CC L | 3,14 | NaN | NaN | 0,52 | 0,48 | NaN | NaN | 1,05 | 13,52 | NaN |
| CC R | 4,25 | NaN | 0,29 | NaN | 0,37 | NaN | NaN | 1,84 | NaN | 132,73 |
| CST L | 0,75 | 0,74 | 1,04 | 0,24 | 0,91 | NaN | 0,70 | 0,62 | 35,68 | 24,29 |
| CST R | 3,89 | 0,75 | NaN | 4,76 | NaN | 5,02 | 0,43 | 7,47 | 7,18 | NaN |
| FA L | NaN | NaN | NaN | 1,40 | NaN | NaN | NaN | NaN | 25,47 | NaN |
| FA R | 1,95 | NaN | 0,89 | NaN | NaN | NaN | NaN | NaN | NaN | 54,65 |
| IFOF L | NaN | 3,87 | NaN | NaN | NaN | 1,76 | NaN | 0,91 | 29,59 | 42,26 |
| IFOF R | NaN | 2,73 | 1,10 | NaN | NaN | NaN | 2,17 | NaN | 15,25 | 26,43 |
| ILF L | NaN | NaN | NaN | 1,09 | 0,84 | NaN | 0,89 | NaN | 27,13 | NaN |
| ILF R | 7,84 | 5,36 | NaN | NaN | NaN | 2,51 | NaN | 5,06 | 23,30 | NaN |
| MLF L | 1,29 | NaN | NaN | 1,63 | NaN | 2,33 | NaN | 1,66 | 18,19 | 72,23 |
| MLF R | 1,45 | 2,74 | 0,59 | NaN | 0,20 | 0,87 | NaN | 0,97 | 23,78 | NaN |
| OCC | NaN | 4,69 | NaN | 1,01 | NaN | 3,53 | 2,62 | 1,48 | NaN | NaN |
| PCC | 6,51 | NaN | NaN | 0,63 | 0,77 | NaN | NaN | NaN | NaN | NaN |
| PTR L | 3,29 | NaN | NaN | NaN | NaN | NaN | NaN | NaN | NaN | 10,09 |
| PMCC | 1,76 | NaN | NaN | NaN | NaN | 3,86 | NaN | 2,43 | 40,80 | 99,40 |
| PSMCC | 5,89 | NaN | NaN | 2,07 | 4,14 | 2,35 | 0,55 | 4,11 | 25,72 | 78,86 |
| STR L | NaN | NaN | NaN | NaN | 1,20 | NaN | NaN | NaN | 14,48 | 241,33 |
| STR R | NaN | NaN | NaN | NaN | NaN | 2,05 | NaN | NaN | 15,10 | 36,93 |
| SMPT L | NaN | 4,00 | NaN | NaN | NaN | NaN | NaN | NaN | 26,41 | NaN |
| SMPT R | NaN | NaN | 3,83 | 2,12 | NaN | 2,07 | 8,25 | 3,16 | 25,97 | NaN |
| TPCB L | NaN | 1,68 | 0,61 | NaN | NaN | 0,65 | 1,09 | NaN | NaN | 40,58 |
| TPCB R | NaN | NaN | NaN | NaN | NaN | 0,79 | NaN | NaN | 9,90 | 36,88 |
| UF L | NaN | NaN | 8,08 | NaN | 7,97 | NaN | 8,51 | NaN | 61,09 | NaN |
| UF R | NaN | 8,58 | 5,88 | NaN | 5,55 | NaN | 6,12 | NaN | 21,22 | NaN |
| WPT L | NaN | 0,95 | 2,57 | NaN | 11,98 | NaN | 1,85 | NaN | 39,19 | 26,38 |
| WPT R | 2,64 | 0,42 | NaN | 2,24 | 1,88 | 2,16 | NaN | 1,42 | NaN | NaN |
| WSLF L | NaN | NaN | 0,75 | 0,32 | NaN | 1,80 | NaN | 0,64 | 26,00 | NaN |
| WSLF R | 5,37 | 2,63 | 2,33 | 0,52 | NaN | NaN | 2,76 | NaN | NaN | 87,21 |

As portrayed in the tables above, the majority of the tracts presented both an increase and decrease in parameters along their trajectory. The following Figure 10 displays some examples of tracts that changed both ways, such as, FA in the Right Corticospinal Tract (4) and MD in the Left Arcuate Fasciculus (1) and others that only presented a single direction of change like AD in the Premotor and supplementary motor CC (2) and RD in the Left Cingulate Cingulum (3).
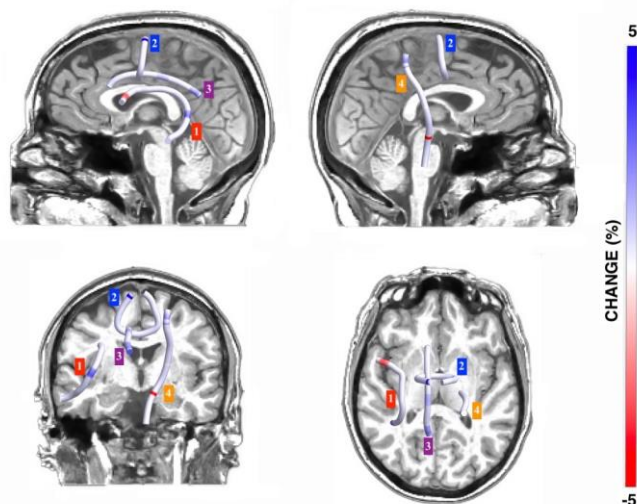


*Figure 10: Mean tracts mapped with respective FA, MD, AD and RD changes*

Focusing on the most notable absolute changes on parameters, we discovered the Left Arcuate Fasciculus presented the biggest increase in FA, with 6,84 %/Gy while the Right Inferior Longitudinal Fasciculus suffered the largest decrease, 7,84 %/Gy. Moreover, regarding the diffusivities, MD increased the most in the Right Corticospinal Tract by 4,76 %/Gy while the biggest decline was registered in the Left Uncinate Fasciculus with 8,08 %/Gy. AD displayed the most prominent increase in the Right Corticospinal Tract, 5,02 %/Gy whereas the Left Whole Pyramidal Tract decreased by 11,98 %/Gy. Moreover, the RD registered the biggest increase in the Right Corticospinal Tract with 7,47 %/Gy and the most notable decrease in the Left Uncinate Fasciculus with 8,51 %/Gy. At last, AFD increased the most in the Left Superior Thalamic Radiation by 241,33 %/Gy, while decreasing by 61,09 %/Gy in the Left Uncinate Fasciculus.

## IV. DISCUSSION

In this study, we analyzed the effect of RT dose delivery on brain microstructure. Current research on dose-tissue interaction has related RT with cognitive decline as a result of GM volume loss [17], demyelination [18] and axonal decay [19]. However, the exact mechanisms that lead to cognitive decline remain unclear. Further information on WM susceptibility to dose is paramount towards developing new dose delivery techniques that reduce cognitive side effects.

We evaluated the change in FA, MD, AD, RD and AFD as a function of the received dose on 31 WM tracts. The results revealed AFD is the most affected parameter by radiation. This metric consistently recorded both the biggest percentage of tract effect and the most notable mean change.

Previous studies regarding WM variation in the presence of dose report a decrease in FA [20] and AFD [21] contrasted by increasing MD, AD and RD [22]. These reports are consistent with our results regarding the general direction of change on these five parameters as a result of dose delivery and is best represented in tracts such as the Left MLF of the PMCC.

However, regional differences have also been recorded. These discrepancies might be related to modelling and the sample size of the study. Although statistical significance has been found and the confidence intervals proved to be narrow, 9 subjects might just not be enough to definitively showcase the effect of radiation on diffusion parameters. The limited number of subjects also implies the imbalance on dose distribution, effect that could be counteracted with more patient inclusions.

We considered a linear model to perform the regression analysis, which might not reflect the real relationship between these parameters. Further development of the model would be beneficial to achieve a more accurate representation.

Moreover, this study was conducted on "low-grade" diffusion data with a basic acquisition of b=1000. New methods, such as multi-shell acquisition [23] allow for a more specific characterization of the brain microestruture, which may improve the modelling of the diffusion signal.

## V. CONCLUSION

In this thesis, we evaluated the radiation-induced changes in the brain microstructure by means of dMRI along 31 WM tracts in a metastatic patient population. The results indicate radiation effects can be traced on diffusion metrics and affect each WM tract in a unique manner. We cannot determine whether these changes lead to cognitive decline, but further neurological exams may reveal the relationship between the changes recorded in this study and cognitive impairment.

## VI. ABBREVIATIONS

| | |
|---|---|
| **AF L** | Arcuate Fasciculus L |
| **AF R** | Arcuate Fasciculus R |
| **CC L** | Cingulate Cingulum L |
| **CC R** | Cingulate Cingulum R |
| **CST L** | CorticoSpinal tract L |
| **CST R** | CorticoSpinal tract R |
| **FA L** | Frontal Aslant L |
| **FA R** | Frontal Aslant R |
| **IFOF L** | Inferior fronto-occipital fasciculus L |
| **IFOF R** | Inferior fronto-occipital fasciculus R |
| **ILF L** | Inferior longitudinal fasciculus L |
| **ILF R** | Inferior longitudinal fasciculus R |
| **MLF L** | Middle longitudinal fasciculus L |
| **MLF R** | Middle longitudinal fasciculus R |
| **OCC** | Occipital CC |
| **PCC** | Parietal CC |
| **PTR L** | Parietal thalamic radiation L |
| **PMCC** | Prefrontal CC |
| **PSMCC** | Premotor and supplementary motor CC |
| **STR L** | Superior thalamic radiation L |
| **STR R** | Superior thalamic radiation R |
| **SMPT L** | Supplementaty motor pyramidal tract L |
| **SMPT R** | Supplementaty motor pyramidal tract R |
| **TPCB L** | TemporalParahippocampal cingulum Bundle L |
| **TPCB R** | TemporalParahippocampal cingulum Bundle R |
| **UF L** | Unciate fasciculus L |
| **UF R** | Unciate fasciculus R |
| **WPT L** | Whole Pyramidal tract L |
| **WPT R** | Whole Pyramidal tract R |
| **WSLF L** | Whole superior longitudinal fasciculus L |
| **WSLF R** | Whole superior longitudinal fasciculus R |

## VII. LAY'S SUMMARY

Radiotherapy (RT) is a cancer treatment therapy based on delivering high levels of radiation to areas affected by tumour cells. However, RT also affects healthy tissue, which leads to cognitive decline in the majority of the patients that undergo the treatment. Current research on the topic of radiation-induced cognitive decline is mostly focused on the volumetric changes that occur within grey matter. However, these studies often overlook the effect that RT has on white matter, which, if measured, could be the key to better understand the mechanisms that lead to cognitive decline after RT. In conclusión, in this study we evaluated the effect of radiation delivery in white matter microestructure.

## VIII. REFERENCES

[1] S. Nagtegaal, S. David, T. Snijders, M. Philippens, A. Leemans and J. Verhoeff, "Effect of radiation therapy on cerebral cortical thickness in glioma patients: Treatment-induced thinning of the healthy cortex," Neuro-Oncology Advances, vol. 2, no. 1, pp. 1-8, 2020.

[2] S. Nagtegaal, S. David, A. van der Boog, A. Leemans and J. Verhoeff, "Changes in cortical thickness and volume after cranial radiation treatment: A systematic review," Radiotherapy and Oncology, vol. 130, no. 2019, pp. 33-42, 2019.

[3] M. Jenkinson, C. Beckmann, T. Behrens, M. Woolrich and S. Smith, ""FSL"," NeuroImage, vol. 62, no. 782, p. 90, 2012.

[4] C. Gaser and R. Dahnke, "CAT-a computational anatomy toolbox for the analysis of structural MRI data," Hbm, vol. 2016, no. 336, p. 48, 2016.

[5] W. Penny, K. Friston, J. Ashburner, S. Kiebel and T. Nichols, Statistical Parametric Mapping: The Analysis of Functional Brain Images, Elsevier, 2007.

[6] A. Leemans, B. Jeurissen, J. Sijbers and D. Jones, "ExploreDTI: A graphical toolbox for processing, analyzing, and visualizing diffusion MR data," Proc Int Soc Magn Reson Med, vol. 17, no. 3537, 2009.

[7] A. De Luca, ""MRIToolkit"," 2019. [Online]. Available: https://github.com/delucaal/MRIToolkit.

[8]    J. Veraart, E. Fieremans and D. Novikov, "Diffusion MRI noise mapping using random matrix theory," Magn Reson Med, vol. 76, no. 5, pp. 1582-1593, 2016.

[9]    J. Andersson, J. Xu, E. Yacoub, E. Auerbach, S. Moeller and K. Ugurbil, "A comprehensive Gaussian Process framework for correcting distortions and movements in diffusion images," Proc ISMRM, vol. 20, p. 2426, 2012.

[10]    A. Leemans and D. Jones, "The B-matrix must be rotated when correcting for subject motion in DTI data," Magnetic Resonance in Medicine, vol. 61, no. 6, pp. 1336-1349, 2009.

[11]    G. Fenghua, A. Leemans, M. Viergever, F. Dell'Acqua and A. De Luca, "Generalized Richardson-Lucy (GRL) for analyzing multi-shell diffusion MRI data," NeuroImage, vol. 218, no. May, p. 116848, 2020.

[12]    B. Fischl, "FreeSurfer," NeuroImage, vol. 62, no. 2, pp. 774-781, 2012.

[13]    A. Radwan, L. Emsell, J. Blommaert, A. Zhylka, S. Kovacs, T. Theys, N. Sollmann, P. Dupont and S. Sunaert, "Virtual brain grafting: Enabling whole brain parcellation in the presence of large lesions," NeuroImage, vol. 229, no. 117731, pp. 1053-8119, 2021.

[14]    C. Destrieux, B. Fischl, A. Dale and E. Halgren, "Automatic parcellation of human cortical gyri and sulci using standard anatomical nomenclature," NeuroImage, vol. 50, no. 1, pp. 1-15, 2010.

[15]    A. Radwan, S. Sunaert, K. Schilling, M. Descoteaux, B. Landman, M. Vandenbulcke, T. Theys, P. Dupont and L. Emsell, "An atlas of white matter anatomy, its variability, and reproducibility based on Constrained Spherical Deconvolution of diffusion MRI," bioRxiv, 2021.

[16]    J. Colby, L. Soderberg, C. Lebel, I. Dinov, P. Thompson and E. Sowell, "Along-tract statistics allow for enhanced tractography analysis," NeuroImage, vol. 59, no. 4, pp. 3227-3247, 2012.

[17]    Y. Lee, H. Cho, W. Lee and W. Sonntag, "Whole brain radiation-induced cognitive impairment: pathophysiological mechanisms and therapeutic targets.," Biomol Ther, vol. 20, no. 4, pp. 357-370, 2012.

[18]    M. Milic and J. Rees, "Acute demyelination following radiotherapy for glioma: a cautionary tale," Pract Neurol, vol. 17, no. 1, pp. 35-38, 2017.

[19]    G. Douaud, S. Jbabdi, T. Behrens, R. Menke, A. Gass and A. Monsch, "DTI measures in crossing-fibre areas: Increased diffusion anisotropy reveals early white matter alteration in MCI and mild Alzheimer's disease," NeuroImage, vol. 55, pp. 880-890, 2011.

[20]    M. Haris, S. Kumar, M. Raj, K. Das, S. Sapru and S. Behari, "Serial diffusion tensor imaging to characterize radiation-induced changes in normal-appearing white matter following radiotherapy in patients with adult low-grade gliomas," Radiat Med - Med Imaging Radiat Oncol, 2008.

[21]    X. Yu, X. Yin and H. Hong, "Increased extracellular fluid is associated with white matter fiber degeneration in CADASIL: in vivo evidence from diffusion magnetic resonance imaging," Fluid Barriers CNS, vol. 18, no. 29, 2021.

[22]    A. Walker, J. Ruzevick, A. Malayeri, D. Rigamonti, M. Lim and K. Redmond, "Postradiation imaging changes in the CNS: how can we differentiate between treatment effect and disease progression?," Futur Oncol, vol. 10, pp. 1277-1297, 2014.

[23]    B. Jeurissen, J. Tournier, T. Dhollander, A. Connelly and J. Sijbers, "Multi-tissue constrained spherical deconvolution for improved analysis of multi-shell diffusion MRI data," NeuroImage, vol. 103, pp. 411-426, 2014.